J Adv Ceram

Research Article

Ultra durable composite steam electrode with cube-shaped $BaZr_{0.85}Y_{0.15}O_{3-\delta}$ facet-boosted efficiency toward advanced protonic ceramic electrolysis cells

Xiaole Yu†, Lin Ge†,✉, Bangze Wu, Zhexiang Yu, Bingyu He, Zhanheng Jin, Zenan Zhao, Han Chen, Yifeng Zheng, Sheng Cui

Cite this article: Yu X, Ge L, Wu B, et al. *J Adv Ceram* 2025, **14**(3): 9221036. https://doi.org/10.26599/JAC.2025.9221036

ABSTRACT: Protonic ceramic electrolysis cells (PCECs) have attracted significant interest because of their efficiency and environmental sustainability in energy conversion. However, their commercial application is hindered by the absence of effective and robust electrodes capable of operating in harsh environments, such as those characterized by high vapor or CO_2 concentrations. In this study, we developed a stable steam electrode composed of $PrBaMn_2O_{5+\delta}$ (PBM) and the durable proton conductor $BaZr_{0.85}Y_{0.15}O_{3-\delta}$ (BZY), which was enhanced with the deposition of PrO_x nano-catalysts. The composite electrode exhibited a low polarization resistance (~0.34 Ω·cm^2 at 600 °C), comparable to that of conventional cobalt-based electrodes. Additionally, extensive testing over hundreds of hours under severe conditions revealed exceptional durability, with no significant degradation observed. Notably, the electrode composited with cube-shaped BZY microcrystals and PBM showed a higher proton conductivity of 2.15×10^{-5} S·cm^{-1} at 500 °C, representing an entire order of magnitude greater than that of the electrode composited with irregular nanosized BZY. In addition, the single cell achieved a superior electrolysis current of 2.0 A·cm^{-2} at 700 °C and 1.3 V. These findings demonstrate the superiority of constructing an innovative interface between the mixed ionic–electronic conductor (MIEC) and the proton conductor. Our work presents a promising strategy for designing durable steam electrodes for PCECs through a rational compositing approach.

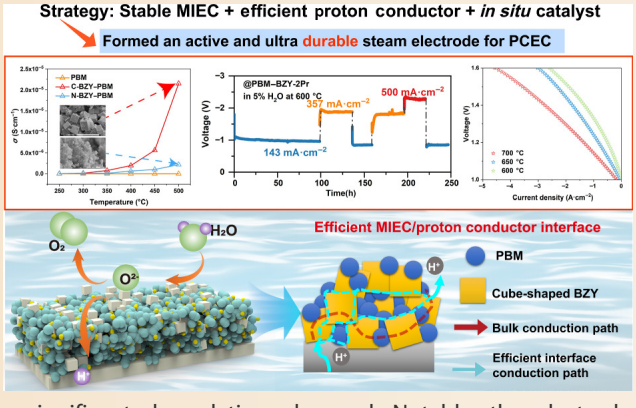

KEYWORDS: protonic ceramic electrolysis cell (PCEC); composite electrode; steam electrode; proton conductivity; cobalt-free electrode

1 Introduction

Solid oxide electrolysis cell (SOEC) is considered the most promising hydrogen production device because of its high efficiency, minimal environmental pollution, and reliable thermodynamic and chemical kinetics [1–6]. However, the high operating temperature (> 700 °C) and humid operating environment (> 20% H_2O) for oxygen ion conductors give rise to expensive original materials and degradation of the steam electrode. Hence, it is vital to decrease the working temperature to an intermediate temperature range (400–600 °C) so that the durability of the steam electrode can be optimized. Unlike traditional SOEC electrolytes ($(Y_2O_3)_{0.08}(ZrO_2)_{0.92}$, etc.), protonic conductor electrolytes ($BaCe_{0.7}Zr_{0.1}Y_{0.1}Yb_{0.1}O_{3-\delta}$, etc.) are used in protonic ceramic electrolysis cells (PCECs) because of their lower activation energy (E_a) [7–11]. Recent advancements have significantly enhanced proton conductivity, improved chemical stability, and optimized the densification sintering process. Unfortunately, the sluggish kinetics of the oxygen evolution reaction (OER) at steam electrodes, coupled with poor durability under high humidity working conditions, severely impedes the broader application of PCECs [12,13].

Traditional mixed-ionic and electronic conductors (MIECs) have been applied in PCEC for decades as one of the most promising electrode materials [8,10,13,14]. For example, $La_{0.6}Sr_{0.4}Co_{0.2}Fe_{0.8}O_{3-\delta}$ (LSCF), a well-known air electrode material in O-SOFCs, was first used as a steam electrode in PCEC [15]. However, the presence of Sr^{3+} in LSCF led to its degradation and

† Xiaole Yu and Lin Ge contributed equally to this work.

College of Materials Science and Engineering, Nanjing Tech University, Nanjing 211816, China.

✉ Corresponding author. E-mail: gelin2013@njtech.edu.cn

Received: November 6, 2024; Revised: January 12, 2025; Accepted: January 13, 2025

the formation of $SrCO_3$ at 600 °C, rendering it unstable. Additionally, other cobalt-based or iron-based perovskite electrodes exhibit excellent catalytic ability and redox behavior due to changes in their valence states. $Ba_{0.5}Sr_{0.5}Co_{0.8}Fe_{0.2}O_{3-\delta}$, a cobalt-rich perovskite for PCFC with excellent electrocatalytic activity for the oxygen evolution reaction (OER), displayed instability in high humidity atmospheres [16–19]. In conclusion, it is difficult for single-phase MIEC electrode materials to maintain high performance and high stability concurrently.

Moreover, multiphase electrodes composed of single-phase MIECs and proton conductors have attracted widespread attention [8,10,14,20,21]. Certain MIECs are composited with $BaZr_{0.8}Y_{0.2}O_{3-\delta}$, enabling the MIECs to facilitate the transfer of both electrons and oxygen ions, while $BaZr_{0.8}Y_{0.2}O_{3-\delta}$ exclusively conducts protons [22]. For example, nano-$LaCoO_{3-\delta}$ [22] and $Ba_{0.5}Gd_{0.8}La_{0.7}Co_{0.2}O_{6-\delta}$ [23], which have been used as PCFC electrodes and, when composited with $BaZr_{0.8}Y_{0.2}O_{3-\delta}$, exhibit excellent electrical performance. Under PCEC operating conditions, the rate-limiting step in the electrochemical process at the steam electrode is the sluggish migration of protons from the electrode to the electrolyte [20,24]. The combination of proton-conducting electrolytes with MIECs enhances proton transfer within the steam electrode and expands the number of electrochemical reaction sites at the interface of MIEC/proton conductor, which is crucial for improving the performance of PCECs. In summary, the incorporation of proton conductors is one of the most effective approaches for promoting the electrochemical performance of steam electrodes for PCECs.

To further explore the electrochemical reaction sites of steam electrodes, extensive research has recently focused on triple-conducting oxides (TCOs) with single-phase structures that can simultaneously facilitate the transfer of protons, oxygen ions, and electrons [25–30]. One notable example is $BaCo_{0.4}Fe_{0.4}Zr_{0.1}Y_{0.1}O_{3-\delta}$ (BCFZY), a well-known single-phase TCO that demonstrates impressive hydration performance at low temperatures for protonic ceramic fuel cells (PCFCs) [26,27,31]. However, while the emphasis on electrochemical performance is critical, it has at times overshadowed the equally important consideration of durability, which may lead to uncertainties in practical applications [32]. Moreover, TCOs used in PCECs often struggle to maintain stability over prolonged periods under harsh operating conditions, particularly in high-humidity environments, due to surface degradation. For example, $PrBa_{0.5}Sr_{0.5}Co_{1.5}Fe_{0.5}O_{5+\delta}$ (PBSCF), another commonly used TCO, has been shown to readily degrade in moist atmospheres, primarily due to the segregation of Ba and Sr to the surface, which triggers concurrent changes in surface structure and chemistry [33–35]. Additionally, single-phase TCOs typically contain transition metal elements such as Co and Fe [36–38]. As the operating temperature increases, the spin state of Co^{3+} transitions to a high-spin state, resulting in a significant increase in the ionic radius and a notably high thermal expansion coefficient (TEC) [39,40]. This elevated TEC can exacerbate the mismatch in the TEC between the electrode and electrolyte interface, ultimately leading to diminished long-term stability [40]. In summary, single-phase TCOs face challenges in achieving both high electrochemical performance and long-term stability concurrently. Consequently, multiphase steam electrodes with triple-conducting functionalities may represent a promising alternative for PCEC applications.

From this perspective, a new strategy for PCEC steam electrodes aimed at achieving excellent electrochemical performance and superior durability is proposed. The stable $PrBaMn_2O_{5+\delta}$ (PBM) electrode is composed of an efficient proton conductor, cube-shaped BZY (C-BZY), and is deposited *in situ* with nano-catalyst PrO_x, resulting in the formation of an ultra-durable heterostructure. $PrBaMn_2O_{5+\delta}$ has demonstrated remarkable durability when used as both fuel electrodes and steam electrodes in SOECs and PCECs [41–44]. The presence of a substantial number of oxygen vacancies, coupled with high electrical conductivity (91.4 $S{\cdot}cm^{-1}$ in air and 8.16 $S{\cdot}cm^{-1}$ in 5% H_2), establishes a solid foundation for its potential as a promising steam electrode material [43]. PrO_x is an active nano-catalyst with superior electrical conductivity and unique redox properties due to its incompletely filled and localized 4f electrons. The electrochemical reactions at the electrodes can be significantly improved because of the high oxygen vacancy-rich surfaces of PrO_x nanoparticles [44–47]. Furthermore, compared with nanosized-BZY (N-BZY), C-BZY has demonstrated superior electrical properties and stability, as established in our previous investigations [48,49]. The composite electrode exhibited exceptional durability under harsh working conditions, with no signs of degradation. Additionally, the composite C-BZY–PBM electrode exhibited faster proton conduction and superior electrical properties than the N-BZY–PBM electrode, revealing our success in designing the interface of composite steam electrodes. Our work presents a promising strategy for developing ultra-durable composite electrodes and provides novel insights into the design of durable steam electrodes for PCECs.

2 Experimental

2.1 Materials synthesis

C-BZY powder was synthesized via the enhanced solid-phase method according to previous reports [48,49]. $Ba(NO_3)_3$ (99.9%, ALADDIN, China) and $(ZrO_2)_{0.92}(Y_2O_3)_{0.08}$ (99.9%, Tosho, Japan) were added to deionized water, dried at 80 °C, and then calcined in air at 800 °C for 2 h to obtain cube-shaped BZY electrolyte powders. Nanosized BZY (N-BZY) powder was prepared by the solid-phase method. Stoichiometric amounts of $BaCO_3$, ZrO_2, and Y_2O_3 (99.9%, ALADDIN, China) were mixed by ball milling, and then sintered in air at 1200 °C for 2 h. $BaZr_{0.1}Ce_{0.7}Y_{0.1}Yb_{0.1}O_{3-\delta}$ (BZCYYb) powder was prepared by a solid-phase method. Stoichiometric amounts of $BaCO_3$, ZrO_2, CeO_2, Y_2O_3, and Yb_2O_3 (99.9%, ALADDIN, China) were mixed by ball milling, and then sintered in air at 1100 °C for 10 h. The PBM electrode powder was synthesized by the solid-phase method. Stoichiometric amounts of Pr_6O_{11}, $BaCO_3$, and MnO_2 were mixed by ball milling, and then sintered in air at 1200 °C for 6 h to obtain the single perovskite $Pr_{0.5}Ba_{0.5}MnO_{3-\delta}$. $PrBaMn_2O_{5+\delta}$ powder was prepared by reducing $Pr_{0.5}Ba_{0.5}MnO_{3-\delta}$ at 800 °C for 1 h in a H_2 atmosphere [44].

2.2 Cell preparation

C-BZY electrolyte pellets were placed in a steel mound with a weight of 0.4 g and a diameter of 14 mm and then pressed at 10 MPa. NiO (3 wt%) was used as a sintering additive for C-BZY electrolyte pellets. Green bodies were sintered at 1450 °C for 10 h to obtain dense electrolyte pellets.

The steam electrodes were fabricated by combining PBM electrode powder with C-BZY electrolyte, followed by impregnation with PrO_x. The steam electrodes were composited at a 6 : 4 ratio for PBM/BZY. The symmetrical cells (PBM–BZY|BZY|PBM–BZY) were fabricated by screen printing and calcination at 1100 °C for 2 h. The half-cells (Ag|BZY|PBM–BZY) were fabricated using the same steps, followed by screen printing with Ag paste and calcination at 750 °C for 15 min. A 0.05 M PrO_x solution was prepared by dissolving analytically pure $Pr(NO_3)_3{\cdot}6H_2O$ in a 1 : 1 mass ratio of deionized water to ethanol.

For each impregnation, 60 μL of PrO_x solution was used. The impregnated PBM–BZY electrodes were named PBM–BZY-*x*Pr (x = 1–3) based on the number of impregnation cycles. The electrodes were calcined at 850 °C after $Pr(NO_3)_3$ infiltration.

The symmetrical cells BZCYYb|C-BZY–PBM|BZCYYb and BZCYYb|N-BZY–PBM|BZCYYb were prepared via the Hebb–Wagner direct current method as follows [50,51]. BZCYYb blocking layers were placed in a steel mold weighing 0.3 g with a diameter of 14 mm, pressed at 100 MPa, and then sintered at 1450 °C for 10 h. The composite electrode slurry was screen-printed and sandwiched between the BZCYYb blocking layers and then calcined at 1200 °C for 2 h. To investigate the proton conduction of the pure PBM electrode, BZCYYb|PBM|BZCYYb symmetrical cells were fabricated via the same procedure.

Single cells, configured as Ni-BZCYYb|BZCYYb|PBM–BZY-PrO_x, were prepared via two main steps. First, the Ni-BZCYYb fuel electrode and BZCYYb electrolyte bilayer film were created using co-pressing and co-sintering processes. NiO powder was physically mixed with BZCYYb electrolyte powder and starch at a ratio of 6 : 4 : 1 to form the fuel electrode powder, which was then pressed into disk-shaped pellets under a pressure of 100 MPa. A small amount of BZCYYb electrolyte was applied to the surface of the fuel electrode and pressed at 200 MPa. The resulting bilayer pellets were sintered at 1450 °C for 5 h in air. Second, the PBM–BZY-PrO_x slurry was screen-printed onto the surface of the electrolyte and subsequently calcined at 1100 °C for 2 h to complete the whole single-cell process, which had an effective electrode area of 0.28 cm^2. The optimal amount of impregnation solution (PBM–BZY-2Pr) was selected to prepare the composite electrode of the single cell, which was then calcined at 850 °C following $Pr(NO_3)_3$ infiltration.

2.3 Characterizations

The phase structure of the materials was analyzed via an X-ray diffractometer (XRD; Cu Kα, 40 kV, 40 mA, 3 kW; Rigaku SmartlabTM, Japan). The microstructures were observed by a scanning electron microscope (SEM; JSM-6360LV, JEOL, Japan) and a transmission electron microscope (TEM; JEM-2100 F, JEOL, Japan). The composition of the electrode was characterized via energy dispersive spectroscopy (EDS). The thermal expansion coefficients (TECs) of the samples were measured using a NETZSCH DIL 402PC dilatometer. The measurements were conducted from room temperature to 800 °C at a heating rate of 5 °C/min. The parameter $\Delta L/L_0$ represents the ratio of the change in length to the initial length during heating.

For electrochemical performance testing, humid air was introduced into the steam electrode to create the right simulation situations. Partial pressures of water vapor (P_{H_2O}) of 0.03, 0.10, 0.20, and 0.3 atm were obtained by bubbling the gas through deionized water at 25, 46, 60, and 70 °C, respectively [52,53]. An electrochemical workstation (CHI660e, Shanghai Chenhua Instrument Co., Ltd., China) was used for electrochemical impedance spectroscopy (EIS) and stability testing at temperatures exceeding 600 °C under different humidity conditions. The frequency range for the EIS measurements was set from 0.01 Hz to 100 kHz. In electrochemical impedance spectroscopy, Z' represents the real part of the impedance, while Z'' represents the imaginary part of the impedance. The data obtained from EIS were analyzed using the relaxation time distribution (DRT) method to study the catalytic effect of PrO_x.

The Hebb–Wagner blocking electrode method was used to analyze the proton conduction of cube-shaped BZY-PBM (C-BZY–PBM), nanosized BZY-PBM (N-BZY–PBM), and pure PBM. The experiments were conducted under extremely low-oxygen partial pressure conditions, ranging from 250 to 500 °C in 50 °C increments. A partial pressure of water vapor (P_{H_2O} of 0.03 atm was maintained by bubbling the gas through deionized water, which was maintained at 25 °C [52,53]. Low oxygen partial pressures (P_{O_2}, approximately 10^{-25} atm) were achieved by mixing H_2, N_2, and vapor, ensuring that ions were the sole charge carriers in the BZCYYb blocking layers (Eq. (1)) [53]. σ_{total}, σ_{proton}, and $\sigma_{electron}$ represent the total conductivity, the protonic conductivity, and the electronic conductivity in Eq. (1), respectively. In addition, BZCYYb has been recognized as a pure proton conductor at temperatures below 500 °C under extremely low oxygen partial pressures (~10^{-25} atm). Therefore, the BZCYYb blocking layers under our test conditions functioned as a double-blocking electrode, effectively preventing the transport of electrons and oxygen ions.

$$\sigma_{total} = \sigma_{proton} + \sigma_{electron} \times (P_{O_2})^{\frac{1}{4}} \quad (1)$$

A constant current (galvanostatic mode) in the range of 1×10^{-4}–1×10^{-7} A was applied between the BZCYYb blocking electrodes using a CHI660e current source, and all voltage drops were recorded as a function of time. Under steady-state conditions, a time-independent voltage signal was observed when electrons and oxygen ions were completely blocked by the BZCYYb blocking electrode [50,51]. Then, only a diffusion-driven protonic current could be detected in the cell. The proton conductivity ($\sigma_{composite\ electrode(proton)}$) can be calculated by Eq. (2):

$$\sigma_{composite\ electrode(proton)} = \frac{L_{composite\ electrode}}{\frac{S \cdot U_{measured}}{I} - \frac{L_{BZCYYb\text{-}1}}{\sigma_{BZCYYb}} - \frac{L_{BZCYYb\text{-}2}}{\sigma_{BZCYYb}}} \quad (2)$$

where $L_{BZCYYb\text{-}1}$, $L_{BZCYYb\text{-}2}$, and $L_{composite\ electrode}$ are the thicknesses of the upper blocking electrode, the lower blocking electrode, and the mixed conducting samples, respectively; S is the active area of the measurement system (0.38 cm^2 in this work); I is the applied constant current; $U_{measured}$ is the final steady-state voltage. The thicknesses of the samples were measured with an ultrasonic thickness gauge (PD-T7, Powerd Technology Beijing Co., Ltd., China) with accuracy of 0.001 mm. The average value of multiple measurements was taken to ensure accuracy. The conductivity (σ_{BZCYYb}) was calculated according to Eq. (3) and from the EIS plot of BZCYYb under extremely low oxygen partial pressures (~10^{-25} atm).

$$\sigma_{BZCYYb} = \frac{L}{R_{ohmic} \times S} \quad (3)$$

3 Results and discussion

3.1 Material characterizations and chemical durability

The XRD patterns of $Pr_{0.5}Ba_{0.5}MnO_{3-\delta}$ and $PrBaMn_2O_{5+\delta}$ powders are shown in Fig. 1(a). The cubic phase and hexagonal phase were observed in $Pr_{0.5}Ba_{0.5}MnO_{3-\delta}$, and the tetragonal phase was observed in $PrBaMn_2O_{5+\delta}$, which is in agreement with Ref. [44]. In addition, the chemical compatibility of PBM–BZY electrode was assessed. No secondary phase was observed after annealing at 1100 °C for 2 h, demonstrating that PBM–BZY is chemically compatible at this temperature, as shown in Fig. 1(a). As shown in Fig. 1(b), the XRD patterns of nano-PrO_x-modified PBM–BZY (6 : 4 in wt%) also demonstrate good chemical compatibility. To assess the stability of the powders, they were treated at 600 °C for

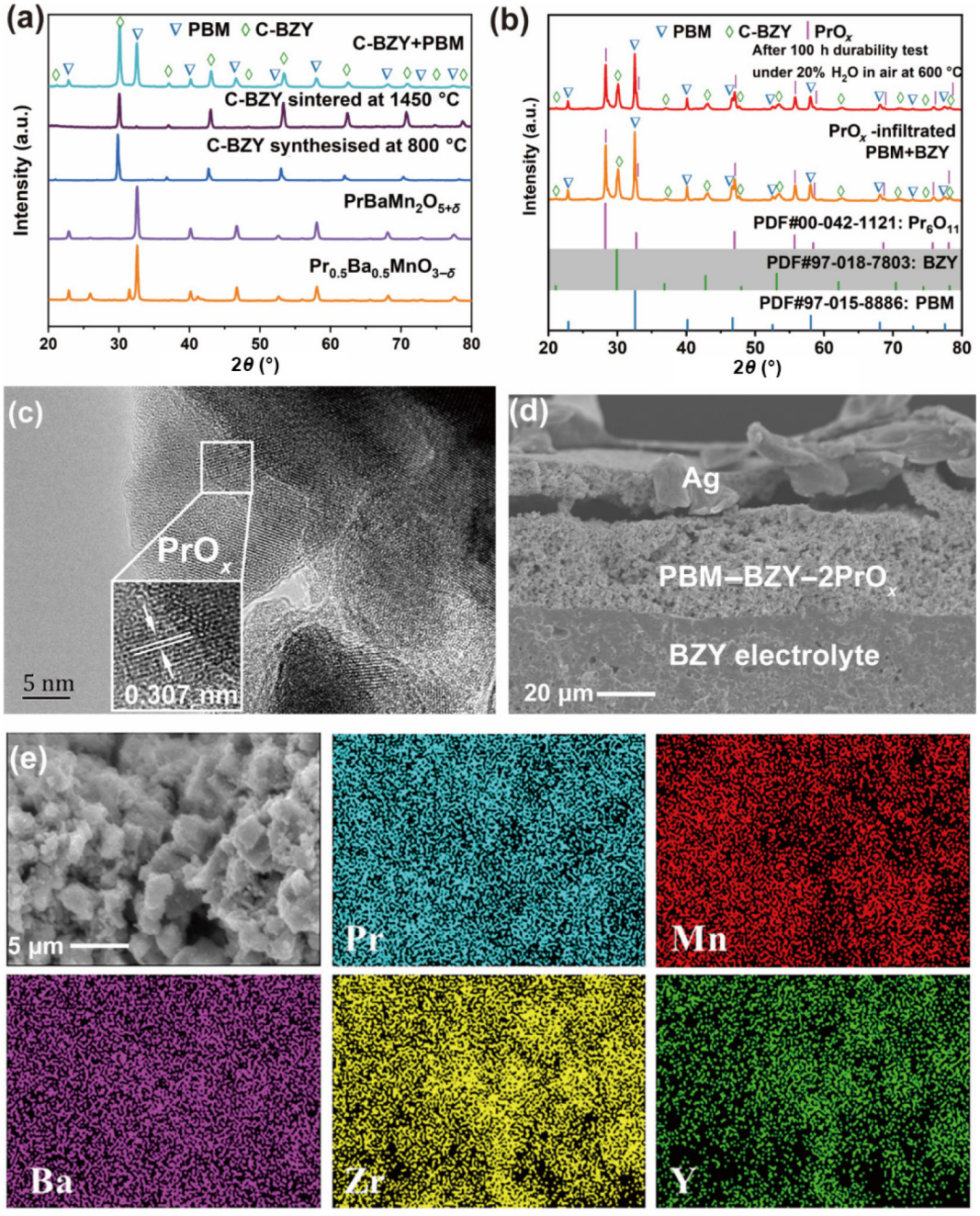

Fig. 1 (a) XRD patterns of PBM after reduction in H_2, C-BZY sintered at 1450 °C, and mixed with C-BZY powders (6 : 4 wt%) after calcination at 1100 °C in air for 2 h; (b) XRD patterns of $Pr(NO_3)_3$-infiltrated PBM–BZY powders before and after durability test in 20% H_2O–air at 600 °C for 100 h; (c) HRTEM images of *in situ* deposited nanoparticles PrO_x before durability test; (d) SEM images of cell cross section with PBM–BZY-2Pr electrode after 100 h stability test under 20% H_2O; (e) EDS elemental mappings of PBM–BZY-2Pr electrode after 100 h stability test under 20% H_2O.

100 h in a steam environment (20% H_2O in air). Compared with those of the untreated powders, the XRD patterns shown in Fig. 1(b) reveal no significant changes, indicating their excellent stability in a high-humidity environment. The high-resolution TEM (HRTEM) analysis is shown in Fig. 1(c). The *d*-spacing is 0.307 nm, which is calculated from the line profile, matching the lattice spacing of Pr_6O_{11}(111) planes (0.315 nm) [45,46] and proving the success of *in-situ* deposition of PrO_x.

Figures 1(d) and 1(e) show SEM images and EDS elemental mapping of PBM–BZY-2Pr electrode after the 100-h stability test. Figure 1(d) shows good adhesion between the electrodes and electrolyte layers, and no obvious lamination is observed. The magnified views in Fig. 1(e) suggest that the PBM particles are uniformly coated on the BZY surface. However, the smaller nanoparticles of PrO_x cannot be directly observed in the SEM image, suggesting that there is no obvious grain growth or agglomeration. Furthermore, the EDS elemental mapping of the PBM–BZY-2Pr electrode after the stability test reveals that all the elements are evenly distributed, and no noticeable element segregation is observed, as shown in Fig. 1(e). The contents of each element are shown in Fig. S1 and Table S1 in the Electronic Supplementary Material (ESM). These results collectively indicate that the PBM–BZY-2Pr electrode exhibits good stability and holds promise as a steam electrode material for PCEC. In conclusion, from the perspective of phase composition and microstructure, the PBM–BZY-*x*Pr composite electrode remained stable after one

hundred hours of durability tests, showing the significant superiority of our electrode design strategy.

3.2 Superiority of efficient MIEC/proton conductor interface

Various approaches, including four-point probe measurement and electromotive force method, have been adopted to investigate the proton conductivity of electrode materials [50,51,54]. In this study, the Hebb–Wagner direct current method was applied with blocking electrodes to evaluate the proton conductivity of the PBM–BZY composite. When the PBM–BZY composite is sandwiched between two BZCYYb dense electrolyte layers and tested at extremely low oxygen partial pressure (~10^{-25} atm), both electron and oxygen ion conduction is blocked, allowing only protons to serve as charge carriers in the PBM–BZY composite electrode [53,55]. Under these conditions, the electrical properties measured reflect only the proton transfer in the PBM–BZY composite material.

As shown in Fig. 2(a), Hebb–Wagner direct current method was employed to evaluate the proton conductivity of C-BZY–PBM, N-BZY–PBM, and pure PBM. Figures 2(b)–2(d) (along with Figs. S2 and S3 in the ESM) illustrate the time dependence of voltage drop under steady-state conditions, where the voltage signals reached saturation within ~100 s. These constant voltage signals represent proton transfer between the two BZCYYb blocking electrodes, with the electrons and oxygen ions being completely blocked. In addition, the microstructure of the BZCYYb blocking electrode is depicted in Figs. S5 and S6 in the ESM, demonstrating that the dense BZCYYb layers are capable of blocking electrons and oxygen ions successfully [55]. Consequently, the practical proton conductivity can be calculated by Eq. (2), with the resistance of BZCYYb blocking electrodes subtracted. The detailed proton conductivities of C-BZY–PBM, N-BZY–PBM, and pure PBM are shown in Fig. 2(e) and Table 1. Notably, C-BZY–PBM exhibited the highest proton conductivity (2.15×10^{-5} S·cm^{-1} at 500 °C) among the samples, representing an 890% increase compared with N-BZY–PBM (2.17×10^{-6} S·cm^{-1} at 500 °C). Compared with that of pure PBM (5.72×10^{-9} S·cm^{-1} at 500 °C), the proton conductivity of C-BZY–PBM improved by several orders of magnitude, highlighting the superior efficiency of cube-shaped BZY in the composite electrode. The Arrhenius plots of C-BZY–PBM, N-BZY–PBM, and pure PBM are shown in Fig. 2(f). Interestingly, the C-BZY–PBM composite electrode has a higher activation energy (0.28 eV) than both N-BZY–PBM (0.18 eV) and pure PBM (0.06 eV), suggesting that proton conduction at the PBM/BZY interface may involve mechanisms beyond the Grotthuss mechanism. Figure 2(g) presents a schematic diagram of the efficient MIEC/proton conductor interface, illustrating that the cube-shaped BZY can provide a

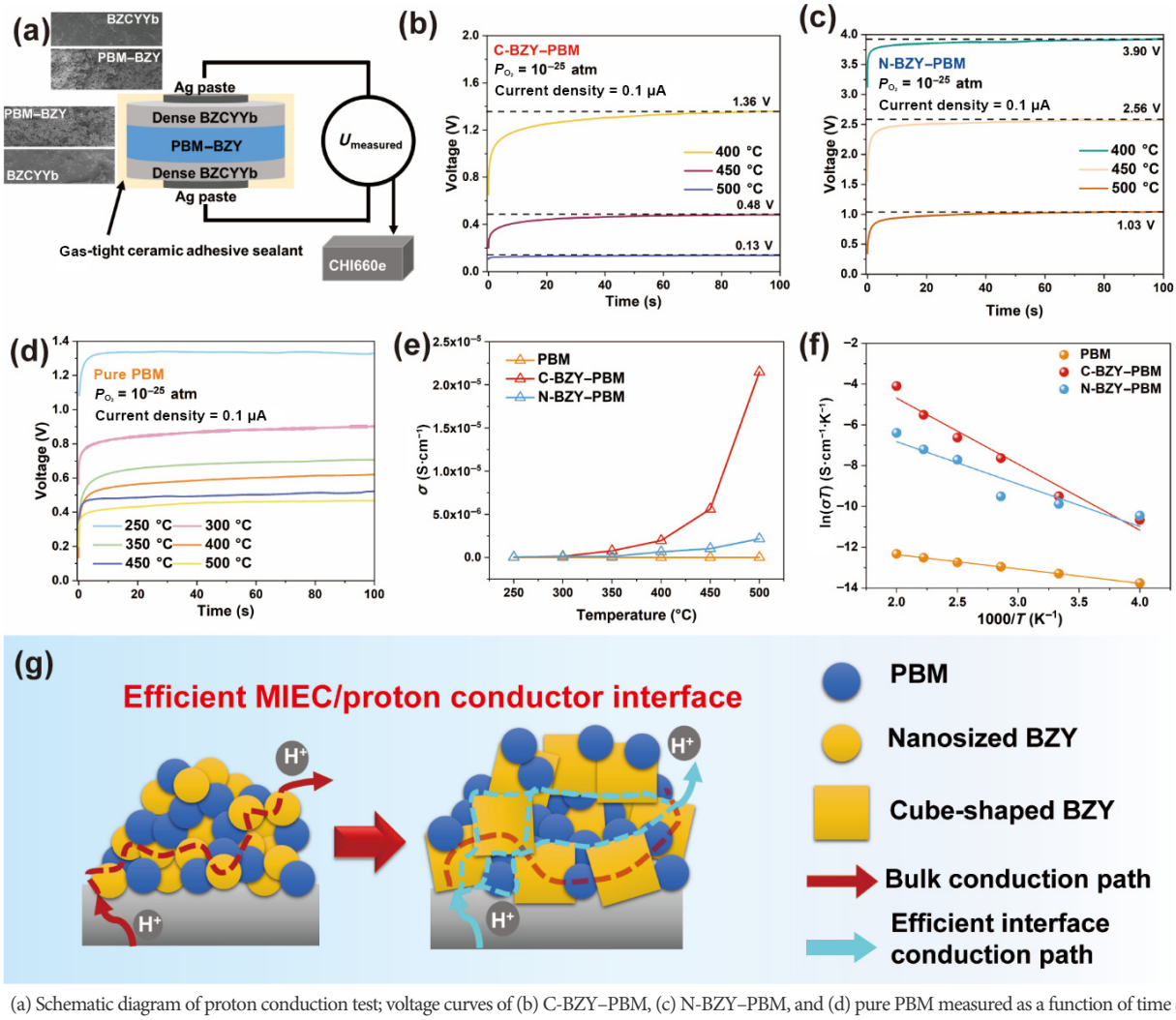

Fig. 2 (a) Schematic diagram of proton conduction test; voltage curves of (b) C-BZY–PBM, (c) N-BZY–PBM, and (d) pure PBM measured as a function of time at 400, 450, and 500 °C at low oxygen partial pressures under galvanostatic conditions; (e) proton conductivity and (f) Arrhenius plots of C-BZY–PBM, N-BZY–PBM, and pure PBM measured by Hebb–Wagner direct current method; (g) schematic diagram of efficient MIEC/proton conductor interface.

direct and efficient pathway for interface transference, which correlates with the observed high proton conductivity. Therefore, the efficient MIEC/proton conductor interface offers a novel strategy for the design of composite electrodes in PCECs.

Recently, the "job-sharing" mechanism has emerged as an innovative theory of ion conduction based on mixed ionic electronic conductors (MIECs) [56–58]. Unlike conventional bulk ion and electron conduction in MIECs, the "job-sharing" interface provides an alternative ion transport pathway at the MIEC/proton conductor interface. Electrons and ions can be accumulated at the periphery of both the MIEC and proton conductor, forming a special space charge layer. This interfacial space charge layer between the MIEC and proton conductor facilitates a rapid transport channel [58]. Nevertheless, it is important to note that the "job-sharing" mechanism is characterized as parallel conduction, which is limited to diffusion across the two-phase interface in alignment with the interface orientation [59]. Notably, the cube-shaped BZY microcrystals, which exhibit a uniform morphology and larger grain size than irregular nanosized BZY, are expected to enhance the efficiency of proton transport in composite electrodes. Our investigation on cube-shaped BZY and nanosized BZY exemplifies efficient MIEC/proton conductor interface design.

3.3 Electrochemical performance of composite electrode

The EIS curves of the steam electrodes PBM, PBM–BZY, and PBM–BZY-*x*Pr (x = 1–3) at 600 °C in steam (3% H_2O) are shown in Figs. 3(a) and 3(b) and Figs. S7 and S8 in the ESM. The electrode area used for the measurements was 0.4 cm^2. The area specific resistance (ASR) decreased from 1.3 to 0.91 Ω·cm^2 with the use of the PBM–BZY composite electrode. Furthermore, the ASR decreased even further after the impregnation of PrO_x. Compared with pristine PBM–BZY, PBM–BZY-2Pr exhibited a 63% reduction in ASR (0.34 Ω·cm^2), highlighting its excellent electrocatalytic activity. With the impregnation of PrO_x, the resistance first increased and then peaked at two impregnation cycles. However, with further impregnation, the resistance increased, likely due to the hindrance caused by excessive PrO_x.

To investigate the catalytic effect of PrO_x on the composite steam electrode, DRT was used to analyze the EIS curves obtained from the PBM, PBM–BZY, and PBM–BZY-2Pr electrodes at 600 °C. As depicted in Fig. 3(c), five distinct peaks can be observed ranging from high frequency (> 10^3 Hz, HF) to intermediate frequency (10^0–10^3 Hz, IF) and low frequency (< 1 Hz, LF), which correspond to five rate-limiting steps during the PBM-based electrode reaction at 600 °C. ASRs of each frequency range are shown in Fig. 3(d) [45]. For the PCEC steam electrode, HF

Table 1 Detailed data of PBM, C-BZY–PBM, and N-BZY–PBM measured from Hebb–Wagner direct current method

Sample	I (μA)	T (°C)	$U_{measured}$ (V)	$L_{electrode}$ (μm)	σ_{proton} (S·cm^{-1})	E_a (eV)
PBM	0.1	400	0.61	100±2	4.31×10^{-9}	0.06
		450	0.52		5.06×10^{-9}	
		500	0.46		5.72×10^{-9}	
C-BZY–PBM	100	400	1.36	101±3	1.97×10^{-6}	0.28
		450	0.48		5.61×10^{-6}	
		500	0.13		2.15×10^{-5}	
N-BZY–PBM	100	400	3.90	103±2	6.62×10^{-7}	0.18
		450	2.56		1.03×10^{-6}	
		500	1.03		2.17×10^{-6}	

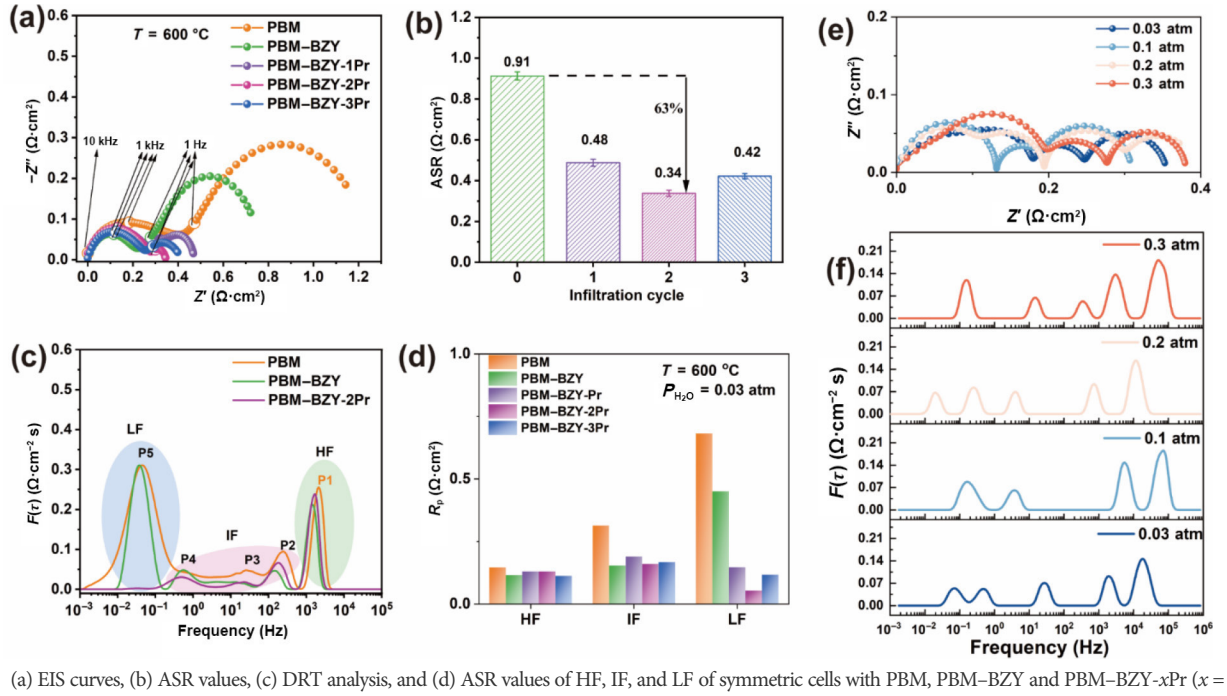

Fig. 3 (a) EIS curves, (b) ASR values, (c) DRT analysis, and (d) ASR values of HF, IF, and LF of symmetric cells with PBM, PBM–BZY and PBM–BZY-*x*Pr (x = 1–3) electrodes in air (3% H_2O) at 600 °C; (e) EIS curves and (f) DRT analysis of PBM–BZY-2Pr electrode under different water vapor concentrations.

typically stands for the transfer of ions and electrons at the interface; IF represents surface oxygen exchange and the diffusion of ions within electrodes; LF corresponds to surface adsorption [46,47]. The composition with BZY and PrO_x significantly decreased the IF and LF peaks. The decrease in the IF process can be attributed to the improved charge transfer facilitated by BZY, while the decrease in the LF process can be attributed to the enhanced surface adsorption caused by nano-PrO_x. The synergistic effect of BZY and PrO_x thus significantly improves the electrochemical performance of the composite electrode, as demonstrated by symmetric cell testing.

Previous studies have shown that ASR of a steam electrode usually increases with increasing water vapor concentration, degrading the electrochemical performance under high-humidity environments. Therefore, the PBM–BZY-2Pr composite electrode was systematically tested under various water vapor concentrations (3%, 10%, 20%, and 30%). As shown in Fig. 3(e), the value of ASR decreases initially and then increases, but the increase remains limited, indicating good stability across a range of water vapor concentrations. As shown in Fig. 3(f), we conducted DRT analysis to further elucidate the electrochemical process under different water vapor concentrations [44]. When P_{H_2O} is 0.1 atm, the intermediate frequency (IF) process, which represents surface oxygen exchange and the diffusion of ions within electrodes, is accelerated because of the catalysis of PrO_x. When P_{H_2O} is 0.2 atm, high frequency (HF) process, which represents the transfer of ions and electrons at the interface, is promoted because of the hydration of cube-shaped BZY. When P_{H_2O} is 0.3 atm, the electrical properties of the composite electrode are similar to those of the composite electrode tested at 0.03 atm P_{H_2O}. In summary, while the water vapor concentration influences the electrochemical processes, the overall ASR remains robust, demonstrating exceptional adaptability to varying humidity.

In addition to electrical conductivity, the ability is crucial for steam electrode to realize superior OER catalytic performance, particularly under high humid environments [32]. To investigate the electron transfer in the composite electrode, the total conductivity was measured at 250 and 800 °C in dry air. As shown in Fig. 4(a), the total conductivity of the pure PBM increased with increasing temperature, from 52.08 to 144.55 S·cm^{-1} [43]. The composite electrode PBM–BZY showed a similar trend, increasing from 1.94 to 18.47 S·cm^{-1}. While the composite electrode displayed lower overall conductivity than the pure PBM, likely due to BZY partially blocking the electron transport pathway, it demonstrated superior proton conductivity, making it more suitable for PCEC steam electrodes.

A significant challenge for steam electrode durability is the thermal expansion coefficient (TEC) mismatch between electrodes and electrolytes [39,40]. Electrolytes such as BZY and BZCYYb typically exhibit TECs of approximately 10×10^{-6} K^{-1}, significantly lower than those of many electrode materials [39]. Co-based electrodes, for example, often exceed 20×10^{-6} K^{-1}, posing a major durability challenge. As shown in Fig. 4(b), the TEC of the PBM reached 13.18×10^{-6} K^{-1}, which was lower than that of traditional Co-based electrodes. Furthermore, the PBM–BZY composite electrode displays an even lower TEC of 11.58×10^{-6} K^{-1}, which is much closer to that of the electrolyte. This reduced TEC is expected to improve electrode–electrolyte interfacial contact and enhance long-term operational durability.

Figure 4(c) shows the polarization resistance of different steam electrodes in symmetrical cells commonly used in PCEC at various steam concentrations. Compared with traditional cobalt-based mixed ionic-electronic conductor (MIEC) electrode materials and common composite electrode materials, the PBM–BZY-2Pr electrode material demonstrated superior performance, which indicates that it is suitable for PCEC steam electrodes.

3.4 Long-term durability testing under harsh working conditions

To assess the short-term durability, a half-cell with the structure "Ag|BZY|PBM–BZY-2Pr" was tested at 600 °C under different water vapor concentrations (30%, 20%, 3%, and 0%). Figure 5(a) shows the cell voltage versus time at a constant current density of 143 mA·cm^{-2} at 600 °C and different steam concentrations. The voltage gradually decreased in a 30% H_2O atmosphere from 0 to 14 h and in a 20% H_2O atmosphere from 24 to 36 h. Subsequently, the 30% H_2O atmosphere was replaced with dry air, and the cell was operated for an additional 10 h (from 14 to 24 h) in dry air, during which the voltage curve remained continuous and stable at approximately –0.5 V. The voltage remained stable during operation in a 3% H_2O atmosphere for 10 h (from 36 to 45 h), indicating that the cell structure was not damaged. Figure 5(b) shows the polarization resistance of the half cell at each stage of the test. After the short-term stability test with different water vapor concentrations, the three-electrode polarization resistance of the electrode remained stable at approximately 0.35 Ω·cm^2, which is consistent with the results of the previous stability test. This demonstrates the durability of PBM–BZY-2Pr electrode under 3%–30% H_2O atmosphere in the short-term test.

Figures 5(c) and 5(d) show the durability test results at different constant current densities of 143, 357, and 500 mA·cm^{-2} at 600 °C for 250 h. The half-cell was operated for 100 h at a current density of 143 mA·cm^{-2}, and the electrode eventually stabilized at a voltage of 0.96 V after the activation process. Subsequently, the working

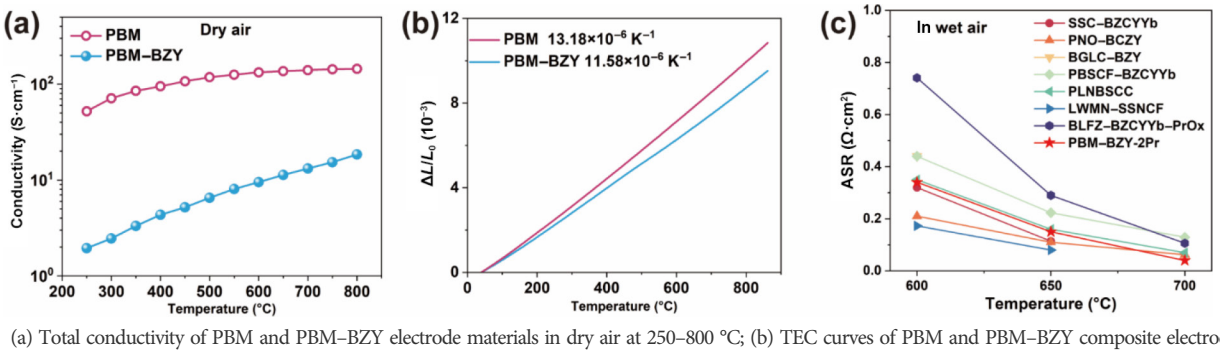

Fig. 4 (a) Total conductivity of PBM and PBM–BZY electrode materials in dry air at 250–800 °C; (b) TEC curves of PBM and PBM–BZY composite electrodes at 40–850 °C; (c) polarization resistance for the different steam electrodes of the symmetrical cells used in PCEC ($Sm_{0.5}Sr_{0.5}CoO_{3-\delta}$–BZCYYb [60], $Pr_2NiO_{4+\delta}$–$BaZr_{0.2}Ce_{0.6}Y_{0.2}O_{3-\delta}$ [61], $Ba_{0.5}Gd_{0.8}La_{0.7}Co_2O_{6-\delta}$–BZY [23], $PrBa_{0.5}Sr_{0.5}Co_{1.5}Fe_{0.5}O_{5+\delta}$–BZCYYb [62], $Pr_{1/6}La_{1/6}Nd_{1/6}Ba_{1/6}Sr_{1/6}Ca_{1/6}CoO_{3-\delta}$ [63], $La_{5.5}W_{0.45}Mo_{0.4}Nb_{0.15}O_{11.25-\delta}$–$Sr_2Sc_{0.1}Nb_{0.1}Co_{1.5}Fe_{0.3}O_{6-\delta}$ [64], $Ba_{0.95}La_{0.05}Fe_{0.8}Zn_{0.2}O_{3-\delta}$–BZCYYb–$PrO_x$ [20]).

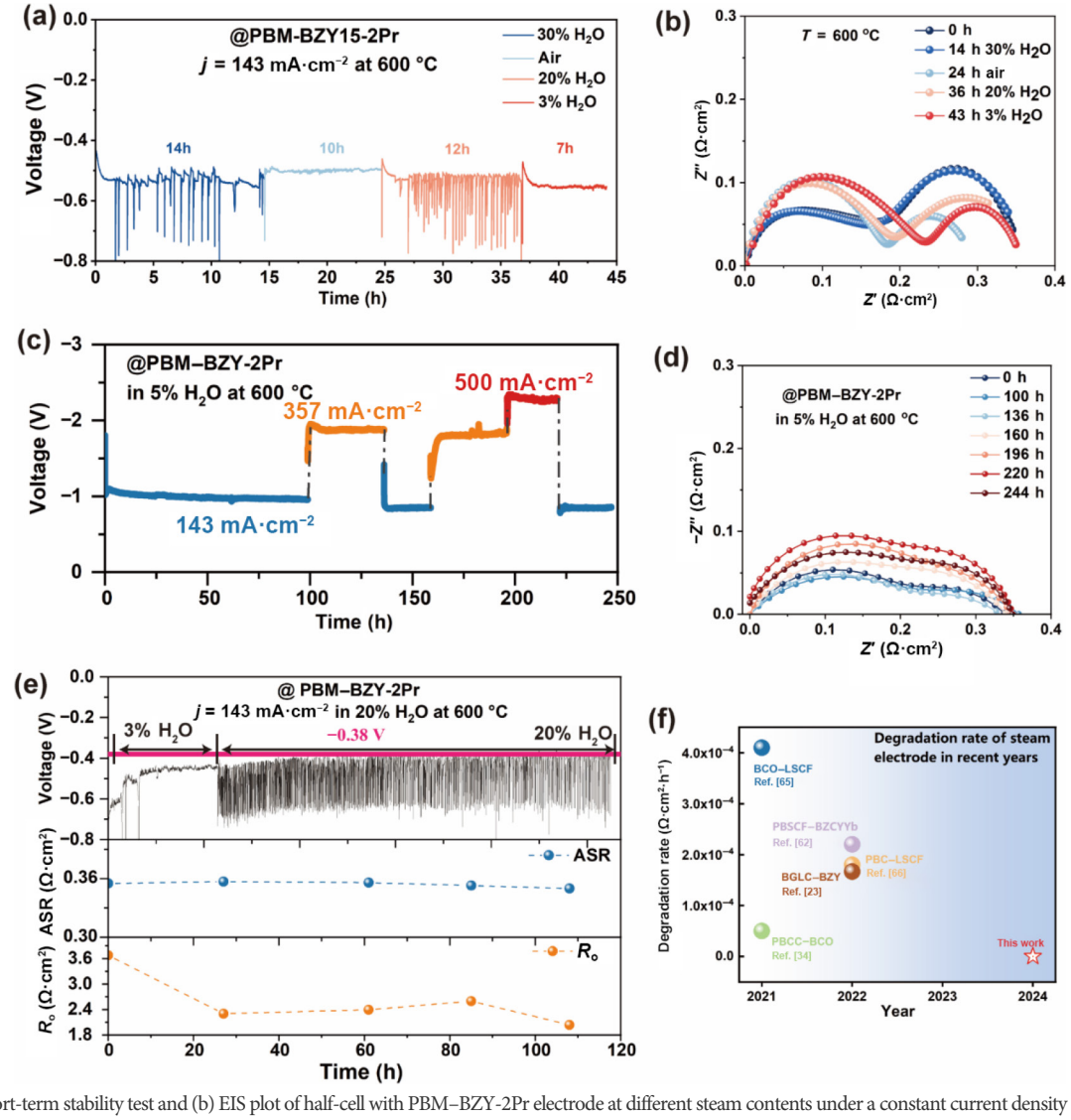

Fig. 5 (a) Short-term stability test and (b) EIS plot of half-cell with PBM–BZY-2Pr electrode at different steam contents under a constant current density of 143 mA·cm^{-2} at 600 °C; (c) 250 h stability test curves and (d) EIS plots of PBM electrode in humidified air (5% H_2O) under different constant current densities of 143, 357, and 500 mA·cm^{-2} at 600 °C; (e) 100 h stability test with PBM–BZY-2Pr electrode in humidified air (20% H_2O) at a constant current density of 143 mA·cm^{-2} at 600 °C and EIS data during 100 h stability test at 600 °C; (f) degradation rates of other steam electrodes in recent years ($BaCoO_{3-\delta}$–$La_{0.6}Sr_{0.4}Co_{0.8}Fe_{0.2}O_{3-\delta}$ [65], $PrBa_{0.8}Ca_{0.2}CoO_{5+\delta}$–$BaCoO_{3-\delta}$ [34], $PrBa_{0.5}Sr_{0.5}Co_{1.5}Fe_{0.5}O_{5+\delta}$–BZCYYb [62], $Ba_{0.5}Gd_{0.8}La_{0.7}Co_2O_{6-\delta}$–BZY [23], and $Pr_{1-x}Ba_xCoO_{3-\delta}$–$La_{0.6}Sr_{0.4}Co_{0.8}Fe_{0.2}O_{3-\delta}$ [66]).

current was increased to 357 mA·cm^{-2}, allowing the cell to operate for an additional 40 h with a stable voltage of approximately 1.9 V. Upon reducing the current, the voltage stabilized at approximately 0.85 V. Interestingly, when operating at the same previous current level, the voltage appeared lower, suggesting that increasing the current further activated the electrode. After multiple cycles of increasing and decreasing current, the voltage remained stable at approximately 0.85 V after continuous operation for 250 h. R_p of the composite electrode exhibited no degradation, which indicates superior durability.

To further investigate the stability of the optimized electrode under high water vapor concentrations, the PBM and PBM–BZY-2Pr electrodes were subjected to a 100-h constant current test (in PCEC mode) at 600 °C (in an environment containing 20% H_2O). Figure S10 in the ESM illustrates the stability test profile of the PBM electrode in humidified air (20% H_2O) at a constant current density of 143 mA·cm^{-2} at 600 °C. The voltage of the cell gradually decreased and stabilized at approximately −0.68 V after a period, indicating that the cell had reached a stable state. Figure S11 in the ESM shows the EIS (including the ohmic resistance, R_o) of the PBM electrode measured in 3 vol% H_2O air at 600 °C before and after the 100-h cell stability test. R_o of the cell decreased from 5.6 to 5 Ω·cm^2 after the test, most likely due to the hydration of BZY electrolyte during the long-term discharge process, which increased the electrolyte conductivity and consequently lowered the R_o value of the half-cell. The excellent durability of the PBM electrode was confirmed by the experimental result that the polarization resistance (R_p) slightly increased from 1.19 to 1.21 Ω·cm^2. The PBM–BZY-2Pr electrode was also tested under the same conditions to examine the influence of BZY and PrO_x on the stability of the PBM electrode. As shown in Fig 5(e) and Fig. S12 in the ESM, the voltage of the cell slowly decreased, indicating an improvement in cell performance. The R_o value decreased from 3.67 to 2.04 Ω·cm^2 before and after the test, representing a reduction of nearly 45%. The significant decrease in R_o may be attributed to the improved electrical contact between the electrolyte and electrode interface during operation. These findings indicate that the composition of BZY and PrO_x does not compromise the stability of the PBM electrode. Furthermore, the low ASR linear degradation rate shows an advantage over other steam electrodes (Fig. 5(f)). Regardless of the atmosphere and current density, the composite

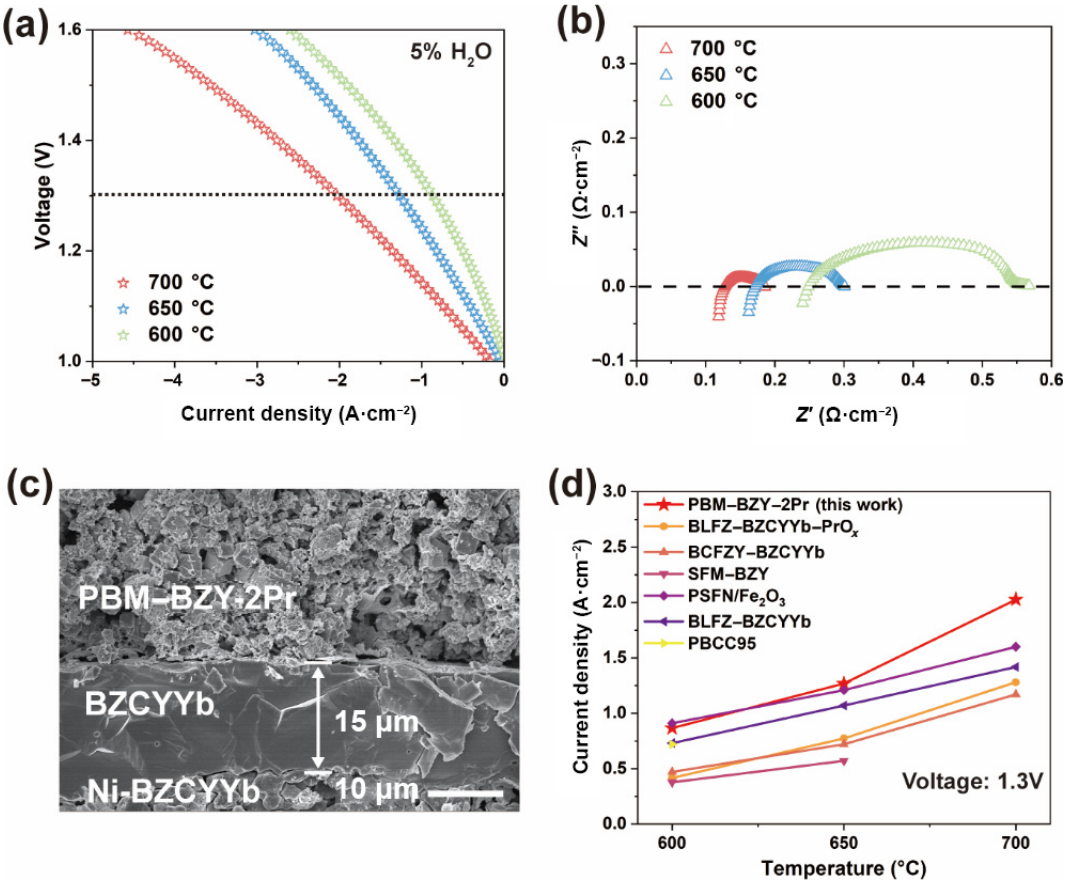

Fig. 6 (a) *I–V* plots for cells measured in PCEC mode at 600–700 °C under H_2 in fuel electrode and 5% H_2O/air in steam electrode; (b) EIS plots of cell in PCEC mode at 600–700 °C; (c) cross-section SEM image of Ni-BZCYYb|BZCYYb|PBM–BZY-2Pr single cell; (d) performance comparisons of cells in PCEC mode ($Ba_{0.95}La_{0.05}Fe_{0.8}Zn_{0.2}O_{3-\delta}$–BZCYYb–$PrO_x$ [20], $BaCo_{0.4}Fe_{0.4}Zr_{0.1}Y_{0.1}O_{3-\delta}$–BZCYYb [67], $Sr_2Fe_{1.5}Mo_{0.5}O_{6-\delta}$–BZY [68], $Pr_{0.4}Sr_{0.6}Fe_{0.9}Nb_{0.1}O_{3-\delta}/Fe_2O_3$ [69], $Ba_{0.95}La_{0.05}Fe_{0.8}Zn_{0.2}O_{3-\delta}$–BZCYYb [70], $(PrBa_{0.8}Ca_{0.2})_{0.95}Co_2O_{6-\delta}$ [71]).

steam electrode remained durable without significant attenuation and even exhibited a decline in ohmic resistance, which showed an incredible activation in the electrolyte.

3.5 Electrochemical performance of single cell

The electrochemical performance of PBM–BZY-2Pr was investigated in a single-cell configuration (Ni-BZCYYb|BZCYYb|PBM–BZY-2Pr) using 5% H_2O humidified air at 600–700 °C. As shown in Fig. 6(a), the single cell with the composite electrode achieved high current densities of 2.02, 1.27, and 0.87 A·cm^{-2} at 700, 650, and 600 °C, respectively, at a voltage of 1.3 V. Figure 6(b) shows corresponding polarization resistance (R_p) values of 0.04, 0.14, and 0.33 Ω·cm^2 at 700, 650, and 600 °C, respectively, which are consistent with the symmetric cell results. In addition, the ohmic resistance (R_o) of a single cell is 0.13, 0.16, and 0.24 Ω·cm^2 at 700, 650, and 600 °C, respectively. Figure 6(c) shows a cross-section image of Ni-BZCYYb|BZCYYb|PBM–BZY-2Pr single cell with an electrolyte thickness of approximately 15 μm. Compared with those of the other composite and traditional steam electrodes, the uniform distributions of PBM and nano PrO_x around the cube-shaped BZY (Fig. 6(c)) resulted in superior electrolysis current densities (Fig. 6(d)). In summary, the PBM–BZY-2Pr composite electrode exhibited both exceptional durability and electrochemical performance, demonstrating the superiority of our compositional and interfacial design strategy. These findings provide a facile and efficient approach for developing ultra-durable steam electrodes for PCECs.

4 Conclusions

In this work, an extremely robust design strategy for composite PCEC steam electrodes was proposed. The durable proton conductor BZY is composited with the stable MIEC PBM, followed by *in-situ* deposition of PrO_x. This system demonstrates notable durability under various working conditions and exhibits comparable electrical performance (0.34 Ω·cm^2 at 600 °C) to that of traditional cobalt-based electrodes. In addition, the single cell with PBM–BZY-2Pr exhibited an exceptional electrolysis current (2.0 A·cm^{-2} at 700 °C and 1.3 V). Unlike other proton conductors used in compositing electrodes, we are the first to incorporate cube-shaped BZY microcrystals into these systems, which feature regular cube shapes that enhance proton conduction at the MIEC/proton conductor interface. The improvement in proton conduction was further validated using the Hebb–Wagner blocking electrode method. Our approach introduces a groundbreaking concept for PCEC composite steam electrodes and offers a novel perspective on interface engineering.

Acknowledgements

This work was supported by the National Natural Science Foundation of China (Nos. 51502136 and 21978133), the Natural Science Foundation of Jiangsu Province (No. BK 20211260), the Priority Academic Program Development (PAPD) of Jiangsu Higher Education Institutions, and the Top-notch Academic Programs Project of Jiangsu Higher Education Institutions (TAPP).

Declaration of competing interest

The authors have no competing interests to declare that are relevant to the content of this article.

Electronic Supplementary Material

Supplementary material is available in the online version of this article at https://doi.org/10.26599/JAC.2025.9221036.

References

[1] Hauch A, Küngas R, Blennow P, *et al.* Recent advances in solid oxide cell technology for electrolysis. *Science* 2020, **370**: eaba6118.

[2] Ghamarinia M, Babaei A, Zamani C, *et al.* Application of the distribution of relaxation time method in electrochemical analysis of the air electrodes in the SOFC/SOEC devices: A review. *Chem Eng J Adv* 2023, **15**: 100503.

[3] Jiang YN, Chen FL, Xia CR. A review on cathode processes and materials for electro-reduction of carbon dioxide in solid oxide electrolysis cells. *J Power Sources* 2021, **493**: 229713.

[4] Xia YY, Deng SL, Sun XZ, *et al.* Progress of symmetrical solid oxide fuel cell. *Adv Ceram* 2023, **44**: 129–141. (in Chinese)

[5] Li XY, Ning XL, Xu CW, *et al.* Research progress and performance optimization strategies of SOFC oxygen ion conductor electrolyte materials. *Adv Ceram* 2023, **44**: 33–42. (in Chinese)

[6] Yin YR, Xiao DD, Wu S, *et al.* A real proton-conductive, robust, and cobalt-free cathode for proton-conducting solid oxide fuel cells with exceptional performance. *SusMat* 2023, **3**: 697–708.

[7] Lei LB, Zhang JH, Yuan ZH, *et al.* Progress report on proton conducting solid oxide electrolysis cells. *Adv Funct Mater* 2019, **29**: 1903805.

[8] Wang YK, Ling YQ, Wang B, *et al.* A review of progress in proton ceramic electrochemical cells: Material and structural design, coupled with value-added chemical production. *Energy Environ Sci* 2023, **16**: 5721–5770.

[9] Medvedev D. Trends in research and development of protonic ceramic electrolysis cells. *Int J Hydrog Energy* 2019, **44**: 26711–26740.

[10] Kasyanova AV, Zvonareva IA, Tarasova NA, *et al.* Electrolyte materials for protonic ceramic electrochemical cells: Main limitations and potential solutions. *Mater Rep Energy* 2022, **2**: 100158.

[11] Liu YY, Luo J, Li C, *et al.* $BaCe_{0.8}Fe_{0.1}Ni_{0.1}O_{3-\delta}$-impregnated Ni-GDC by phase-inversion as an anode of solid oxide fuel cells with on-cell dry methane reforming. *J Adv Ceram* 2024, **13**: 834–841.

[12] Liu F, Ding D, Duan CC. Protonic ceramic electrochemical cells for synthesizing sustainable chemicals and fuels. *Adv Sci* 2023, **10**: 2206478.

[13] Wang QJ, Ricote S, Chen M. Oxygen electrodes for protonic ceramic cells. *Electrochim Acta* 2023, **446**: 142101.

[14] Tarutin AP, Filonova EA, Ricote S, *et al.* Chemical design of oxygen electrodes for solid oxide electrochemical cells: A guide. *Sustain Energy Technol Assess* 2023, **57**: 103185.

[15] Wu L, Sun JQ, Qi HY, *et al.* Boosting steam tolerance and electrochemical performance of an $La_{0.6}Sr_{0.4}Co_{0.2}Fe_{0.8}O_{3-\delta}$-based air electrode for protonic ceramic electrochemical cells. *J Mater Chem A* 2024, **12**: 25979–25987.

[16] Lin Y, Ran R, Zheng Y, *et al.* Evaluation of $Ba_{0.5}Sr_{0.5}Co_{0.8}Fe_{0.2}O_{3-\delta}$ as a potential cathode for an anode-supported proton-conducting solid-oxide fuel cell. *J Power Sources* 2008, **180**: 15–22.

[17] Zhou W, Ran R, Shao ZP. Progress in understanding and development of $Ba_{0.5}Sr_{0.5}Co_{0.8}Fe_{0.2}O_{3-\delta}$-based cathodes for intermediate-temperature solid-oxide fuel cells: A review. *J Power Sources* 2009, **192**: 231–246.

[18] Wei B, Lü Z, Li SY, *et al.* Thermal and electrical properties of new cathode material $Ba_{0.5}Sr_{0.5}Co_{0.8}Fe_{0.2}O_{3-\delta}$ for solid oxide fuel cells. *Electrochem Solid-State Lett* 2005, **8**: A428.

[19] Chen KF, Yang HR, Chen ZY, *et al.* Enabling stable operation of $Ba_{0.5}Sr_{0.5}Co_{0.8}Fe_{0.2}O_{3-\delta}$ based multiphase nanocomposite cathode for efficient intermedium temperature solid oxide fuel cells. *Ceram Int* 2024, **50**: 46822–46830.

[20] Jing JM, Lei Z, Xue YH, *et al.* Constructing highly active and durable oxygen electrode by nanoengineering for reversible protonic ceramic cell. *Energy Storage Mater* 2024, **72**: 103694.

[21] Wei B, Zhe L, Huang XQ, *et al.* Synthesis, electrical and electrochemical properties of $Ba_{0.5}Sr_{0.5}Zn_{0.2}Fe_{0.8}O_{3-\delta}$ perovskite oxide for IT-SOFC cathode. *J Power Sources* 2008, **176**: 1–8.

[22] Wang QJ, Tong XF, Ricote S, *et al.* Nano-$LaCoO_3$ infiltrated $BaZr_{0.8}Y_{0.2}O_{3-\delta}$ electrodes for steam splitting in protonic ceramic electrolysis cells. *Adv Powder Mater* 2022, **1**: 100003.

[23] Wang QJ, Ricote S, Wang Y, *et al.* $Ba_{0.5}Gd_{0.8}La_{0.7}Co_2O_{6-\delta}$ infiltrated $BaZr_{0.8}Y_{0.2}O_{3-\delta}$ composite oxygen electrodes for protonic ceramic cells. *J Electrochem Soc* 2022, **169**: 014513.

[24] Abdullah Umer M, Cheng CY, Lai BR, *et al.* Growth of $Gd_{0.3}Ca_{2.7}Co_{3.82}Cu_{0.18}O_{9-\delta}$–$BaCe_{0.6}Zr_{0.2}Y_{0.2}O_{3-\delta}$ bulk heterojunction cathode interlayer by pulsed laser deposition for enhancing protonic solid oxide fuel cell performance. *Appl Surf Sci* 2023, **638**: 158139.

[25] Ding HP, Wu W, Jiang C, *et al.* Self-sustainable protonic ceramic electrochemical cells using a triple conducting electrode for hydrogen and power production. *Nat Commun* 2020, **11**: 1907.

[26] Park K, Saqib M, Lee H, *et al.* Water-mediated exsolution of nanoparticles in alkali metal-doped perovskite structured triple-conducting oxygen electrocatalysts for reversible cells. *Energy Environ Sci* 2024, **17**: 1175–1188.

[27] Duan CC, Kee R, Zhu HY, *et al.* Highly efficient reversible protonic ceramic electrochemical cells for power generation and fuel production. *Nat Energy* 2019, **4**: 230–240.

[28] Dai HL, Boulfrad S, Chu XR, *et al.* $La_{0.5-x}Sc_xSr_{0.5}MnO_{3-\delta}$ cathodes for proton-conducting solid oxide fuel cells: Taking advantage of the secondary phase. *J Adv Ceram* 2024, **13**: 1759–1770.

[29] Li YF, Xu YS, Yin YR, *et al.* Entropy engineering design of high-performing lithiated oxide cathodes for proton-conducting solid oxide fuel cells. *J Adv Ceram* 2023, **12**: 2017–2031.

[30] Zhou R, Yin YR, Dai HL, *et al.* Attempted preparation of $La_{0.5}Ba_{0.5}MnO_{3-\delta}$ leading to an *in situ* formation of manganate nanocomposites as a cathode for proton-conducting solid oxide fuel cells. *J Adv Ceram* 2023, **12**: 1189–1200.

[31] Tarutina LR, Gordeeva MA, Matkin DE, *et al.* Why do $BaCo_{0.4}Fe_{0.4}Zr_{0.1}Y_{0.1}O_{3-\delta}$-derived complex oxides become one of the most promising electrodes for protonic ceramic electrochemical cells. An explanatory review. *Chem Eng J* 2024, **490**: 151615.

[32] Chen X, Yu N, Song YF, *et al.* Synergistic bulk and surface engineering for expeditious and durable reversible protonic ceramic electrochemical cells air electrode. *Adv Mater* 2024, **36**: 2403998.

[33] Liu F, Deng H, Diercks D, *et al.* Lowering the operating temperature of protonic ceramic electrochemical cells to < 450 °C. *Nat Energy* 2023, **8**: 1145–1157.

[34] Zhou YC, Liu EZ, Chen Y, *et al.* An active and robust air electrode for reversible protonic ceramic electrochemical cells. *ACS Energy Lett* 2021, **6**: 1511–1520.

[35] Chen KF, Jiang SP. Surface segregation in solid oxide cell oxygen electrodes: Phenomena, mitigation strategies and electrochemical properties. *Electrochem Energy Rev* 2020, **3**: 730–765.

[36] Dai HL, Du HZ, Boulfrad S, *et al.* Manipulating Nb-doped $SrFeO_{3-\delta}$ with excellent performance for proton-conducting solid oxide fuel cells. *J Adv Ceram* 2024, **13**: 579–589.

[37] Yin YR, Zhou YB, Gu YY, *et al.* Successful preparation of $BaCo_{0.5}Fe_{0.5}O_{3-\delta}$ cathode oxide by rapidly cooling allowing for high-performance proton-conducting solid oxide fuel cells. *J Adv Ceram* 2023, **12**: 587–597.

[38] Yin YR, Zhang SQ, Wang A, *et al.* Rational design of $PrBaFe_2O_{6-\delta}$-based cathodes for protonic ceramic fuel cells. *J Adv Ceram* 2024, **13**: 1600–1610.

[39] Yu ZX, Ge L, Ni Q, *et al.* Superior durability and activity of a benchmark triple-conducting cathode by tuning thermo–mechanical

compatibility for protonic ceramic fuel cells. *Adv Funct Mater* 2024, **34**: 2309698.
[40] Zhang Y, Chen B, Guan DQ, *et al.* Thermal-expansion offset for high-performance fuel cell cathodes. *Nature* 2021, **591**: 246–251.
[41] Hua B, Yan N, Li M, *et al.* Anode-engineered protonic ceramic fuel cell with excellent performance and fuel compatibility. *Adv Mater* 2016, **28**: 8922–8926.
[42] Pang SL, Xu J, Su YJ, *et al.* The role of A-site cation size mismatch in tune the catalytic activity and durability of double perovskite oxides. *Appl Catal B—Environ* 2020, **270**: 118868.
[43] Sengodan S, Choi S, Jun A, *et al.* Layered oxygen-deficient double perovskite as an efficient and stable anode for direct hydrocarbon solid oxide fuel cells. *Nat Mater* 2015, **14**: 205–209.
[44] Gu YH, Zhang YL, Zheng YF, *et al.* $PrBaMn_2O_{5+\delta}$ with praseodymium oxide nanocatalyst as electrode for symmetrical solid oxide fuel cells. *Appl Catal B—Environ* 2019, **257**: 117868.
[45] Ge L, Sun KQ, Gu YH, *et al.* Boosting the performance of conventional air electrodes for solid oxide cells by *in situ* loading of nano praseodymium oxide. *Energy Convers Manag* 2021, **249**: 114873.
[46] Sun KQ, Yu ZX, Ni Q, *et al.* Highly durable Sr-doped $LaMnO_3$-based cathode modified with Pr_6O_{11} nano-catalyst for protonic ceramic fuel cells based on Y-doped $BaZrO_3$ electrolyte. *J Eur Ceram Soc* 2022, **42**: 4266–4274.
[47] Nam S, Kim J, Kim H, *et al.* Revitalizing oxygen reduction reactivity of composite oxide electrodes via electrochemically deposited PrO_x nanocatalysts. *Adv Mater* 2024, **36**: 2307286.
[48] Ge L, Jiao JH, zhu ZC, *et al.* A facile method to fabricate proton-conducting $BaZr_{0.85}Y_{0.15}O_{3-\delta}$ electrolyte with a large grain size and high conductivity. *Ceram Int* 2019, **45**: 24946–24952.
[49] Jiao JH, Li Q, Gu YH, *et al.* Effect of $BaOB_2O_3$ composite sintering aid on sinterability and electrical property of $BaZr_{0.85}Y_{0.15}O_{3-\delta}$ ceramic. *Ceram Int* 2019, **45**: 13679–13684.
[50] Miruszewski T, Dzierzgowski K, Winiarz P, *et al.* Hebb–Wagner polarization method for determining the oxygen ion conductivity in barium cerate-zirconate. *J Mater Chem A* 2022, **10**: 7218–7227.
[51] Miruszewski T, Strandbakke R, Dzierzgowski K, *et al.* A modified DC Hebb–Wagner polarization method for determining the partial protonic electrical conductivity in mixed-conducting $BaGd_{0.3}La_{0.7}Co_2O_{6-\delta}$. *J Mater Chem A* 2024, **12**: 13488–13497.
[52] Yu XL, Zhou XK, Wu BZ, *et al.* Two birds with one stone: Benefits of sintering additives on sinterability and electrical property of new protonic ceramic fuel cell electrolyte $SrSn_{0.8}Sc_{0.2}O_{3-\delta}$. *Ceram Int* 2024, **50**: 40216–40225.
[53] Jiang LL, Han DL. Protonic and electronic hole conductivity of grain interior and grain boundaries in $BaZr_{0.9}Y_{0.1}O_{3-\delta}$: Effect from sample processing. *Chem Eng J* 2024, **486**: 150309.
[54] Huang Y, Qiu RM, Lian WC, *et al.* Review: Measurement of partial electrical conductivities and transport numbers of mixed ionic-electronic conducting oxides. *J Power Sources* 2022, **528**: 231201.
[55] Guo H, Li YF, Jiang LL, *et al.* Transport properties of the Ba(Zr,Ce,Y,Yb)$O_{3-\delta}$ proton conductor: The real role of co-substitution of Y and Yb. *J Mater Chem A* 2024, **12**: 5875–5884.
[56] Riedl C, Schmid A, Nenning A, *et al.* Outstanding oxygen reduction kinetics of $La_{0.6}Sr_{0.4}FeO_{3-\delta}$ surfaces decorated with platinum nanoparticles. *J Electrochem Soc* 2020, **167**: 104514.
[57] Chen CC, Fu LJ, Maier J. Synergistic, ultrafast mass storage and removal in artificial mixed conductors. *Nature* 2016, **536**: 159–164.
[58] Chen SH, Chen CC. Space charge effects in mixed ionic-electronic conducting electrodes for solid-state batteries. *Phys Chem Chem Phys* 2024, **26**: 24689–24698.
[59] Chen CC, Maier J. Space charge storage in composites: Thermodynamics. *Phys Chem Chem Phys* 2017, **19**: 6379–6396.
[60] Seong A, Jeong D, Kim M, *et al.* Performance comparison of composite cathode: Mixed ionic and electronic conductor and triple ionic and electronic conductor with $BaZr_{0.1}Ce_{0.7}Y_{0.1}Yb_{0.1}O_{3-\delta}$ for highly efficient protonic ceramic fuel cells. *J Power Sources* 2022, **530**: 231241.
[61] Li WY, Guan B, Ma L, *et al.* High performing triple-conductive $Pr_2NiO_{4+\delta}$ anode for proton-conducting steam solid oxide electrolysis cell. *J Mater Chem A* 2018, **6**: 18057–18066.
[62] Bai H, Zhang YH, Chu JM, *et al.* Oxygen electrode $PrBa_{0.5}Sr_{0.5}Co_{1.5}Fe_{0.5}O_{5+\delta}$–$BaZr_{0.1}Ce_{0.7}Y_{0.1}Yb_{0.1}O_{3-\delta}$ with different composite proportions for proton-conducting solid oxide electrolysis cells. *ACS Appl Mater Inter* 2023, **15**: 38581–38591.
[63] Liu ZQ, Tang ZJ, Song YF, *et al.* High-entropy perovskite oxide: A new opportunity for developing highly active and durable air electrode for reversible protonic ceramic electrochemical cells. *Nano–Micro Lett* 2022, **14**: 217.
[64] Wang XY, Fei MJ, Zhou C, *et al.* Enhanced proton conductivity and CO_2-tolerance of intermediate-temperature protonic ceramic fuel cell with lanthanum tungstate-based composite cathode. *Compos Part B—Eng* 2023, **253**: 110565.
[65] Zhou YC, Zhang WL, Kane N, *et al.* An efficient bifunctional air electrode for reversible protonic ceramic electrochemical cells. *Adv Funct Mater* 2021, **31**: 2105386.
[66] Niu YH, Zhou YC, Zhang WL, *et al.* Highly active and durable air electrodes for reversible protonic ceramic electrochemical cells enabled by an efficient bifunctional catalyst. *Adv Energy Mater* 2022, **12**: 2103783.
[67] Lee H, Jung H, Kim C, *et al.* Enhanced electrochemical performance and durability of the $BaCo_{0.4}Fe_{0.4}Zr_{0.1}Y_{0.1}O_{3-\delta}$ composite cathode of protonic ceramic fuel cells via forming nickel oxide nanoparticles. *ACS Appl Energy Mater* 2021, **4**: 11564–11573.
[68] Lei LB, Tao ZT, Wang XM, *et al.* Intermediate-temperature solid oxide electrolysis cells with thin proton-conducting electrolyte and a robust air electrode. *J Mater Chem A* 2017, **5**: 22945–22951.
[69] Wang Z, Xiao YC, Zhang Y, *et al.* A novel chemical composite strategy for synergistically enhancing the activity and stability of strontium-containing air electrode for protonic ceramic cells. *Chem Eng J* 2024, **490**: 151911.
[70] Jing JM, Lei Z, Zheng ZW, *et al.* Triple conducting perovskite $Ba_{0.95}La_{0.05}Fe_{0.8}Zn_{0.2}O_{3-\delta}$ as oxygen electrode for reversible protonic ceramic cells. *Int J Hydrog Energy* 2023, **48**: 9037–9045.
[71] Tang W, Ding HP, Bian WJ, *et al.* Understanding of A-site deficiency in layered perovskites: Promotion of dual reaction kinetics for water oxidation and oxygen reduction in protonic ceramic electrochemical cells. *J Mater Chem A* 2020, **8**: 14600–14608.